Magnetism and magneto-structural effects in transition-metal sulphides

Magnetism and magneto-structural effects in transition-metal sulphides

D Hobbs†‡ and J Hafner‡§

† Institut für Theoretische Physik, Technische Universität Wien, Wiedner Hauptstraße 8–10/136,
A-1040 Wien, Austria
‡ Centre for Computational Material Science, Sensengasse 8, A-1090 Wien, Austria
§ Institut für Material Physik, Universität Wien, Sensengasse 8, A-1090 Wien, Austria

Abstract. Recent density-functional studies of the structural and electronic properties of a wide range of transition-metal sulphides (Raybaud P, Kresse G, Hafner J and Toulhoat H 1997 *J. Phys.: Condens. Matter* **9** 11 085, 11 107) are extended to consider the effect of magnetic ordering in sulphides formed by 3d transition metals. We find that CrS is well described as an itinerant antiferromagnet and that the magnetic ordering leads to a substantial increase of the equilibrium volume and a reduction in the axial ratio of the NiAs-type lattice. MnS(NaCl structure) is correctly described as a high-spin type-II antiferromagnet (AFM) with a very large magneto-volume effect, but the semiconducting gap is underestimated—probably due to the neglect of correlation effects. Correlation effects are also important for stabilizing the high-spin AFM type-III state of MnS_2 over the low-spin state. The phase transitions between non-magnetic (NM) NiAs-type FeS and antiferromagnetic troilite are well described by spin-density-functional theory, but the formation of a semiconducting gap and the magnitude of the magnetic moments and exchange splitting can be explained only by postulating correlation effects of intermediate strength. FeS_2(pyrite or marcasite) and CoS are predicted to be non-magnetic, while cubic CoS_2 is well characterized as an itinerant weak ferromagnet. NiS and NiS_2 are predicted to be non-magnetic by local spin-density theory, in contrast to experiment.

1. Introduction

Transition-metal sulphides have found many technological applications, ranging from lubrication to the use as catalysts in sulpho-reductive hydrotreating processes in the petroleum refining industry [1]. In addition, transition-metal sulphides are also of fundamental scientific interest. The sulphides of the transition metals are intermediate between the transition-metal oxides, whose properties are determined by strong electronic correlation effects [2], and the transition-metal selenides showing a variety of electronically induced structural phase transitions (including the formation of incommensurate phases [3]). The combined scientific and technological importance of these materials has motivated a substantial research effort directed towards an understanding of their properties at an atomistic level, starting with the pioneering work of Wilson and Yoffe [4], Huisman *et al* [5], and Mattheis [6].

In a recent series of papers, Raybaud *et al* [7,8] have presented comprehensive studies of the structural and cohesive properties of more than thirty transition-metal sulphides (TMS) within the local density approximation (LDA) [9, 10]. Their calculations revealed a pronounced trend towards overbinding which manifested itself in a prediction of too-small atomic volumes and too-large cohesive energies. Additionally, the work has shown that non-local corrections to the

LDA, namely the generalized-gradient approximation (GGA) [11], can correct the overbinding and lead to accurate prediction of crystal structures and cohesive energies.

Nevertheless, for many of the 3d-band TMS, agreement with experiment is still rather poor, with errors in the predicted equilibrium volume approaching 25% in some cases. The obvious solution to this dilemma is to consider the magnetic properties of these materials which have, to our knowledge, been left unstudied within this context. Magneto-volume and magneto-structural effects can play an important role in accurately predicting the atomic volume and crystal structure of these materials.

We have limited our studies to the 3d-band monosulphides and disulphides as they are generally known to be magnetic and exhibit the poorest agreement with experiment in the studies of Raybaud *et al* [7, 8]. In section 2 we briefly review the theory used to solve the Kohn–Sham equations and the computational approach employed in this paper. Section 3 discusses the structural, electronic and magnetic properties of each material and, finally, in section 4 our conclusions are presented.

2. Theory

2.1. Method

Kohn–Sham density-functional theory has proved to be a very successful and, particularly when used in conjunction with a plane-wave basis and pseudopotentials, also a very efficient tool for studying the properties of materials at a microscopic level. Standard norm-conserving pseudopotentials are however computationally expensive to use, particularly for the first-row elements, transition metals and rare-earth elements. This problem has been circumvented to some extent by the use of ultrasoft pseudopotentials [12–14], which relaxes the norm-conserving condition that is usually imposed on the pseudo-charge density. This approach has allowed the first-row and transition-metal elements to be treated efficiently. However, substantial difficulties persist for the early 3d transition metals where the overlap of the 3d valence charge density with the 3p 'semi-core states' cannot be neglected. It has been demonstrated [15] that, for the magnetic phases of these materials in particular, the 'non-linear core corrections' introduced by Louie *et al* [16] to correct for the inherent non-linearity of the exchange–correlation functional are insufficient. Due to the rather localized nature of the spin density, the exchange and correlation must be treated on the basis of the full all-electron charge and spin densities. This is possible using an approach proposed by Blöchl [17] combining ideas from pseudopotentials and linearized-augmented-plane-wave (LAPW) methods into an elegant framework known as the projected-augmented-wave (PAW) method. Very recently Kresse and Joubert [18] demonstrated that there is a one-to-one correspondence between ultra-soft pseudopotentials and the PAW approach, and adapted the technique to metallic systems. The advantage of the PAW technique is that it is an all-electron approach, and provides the full wavefunctions that are not directly accessible with the pseudopotential approach. Additionally, the potential is determined from the full charge density.

The all-electron wavefunction $|\Psi_m\rangle$ is generated from the pseudo-wavefunction $|\tilde{\Psi}_m\rangle$ using

$$|\Psi_m\rangle = |\tilde{\Psi}_m\rangle + \sum_i (|\phi_i\rangle - |\tilde{\phi}_i\rangle)\langle\tilde{p}_i|\tilde{\Psi}_m\rangle. \tag{1}$$

The all-electron partial waves $|\phi_i\rangle$ are obtained by radially integrating the Schrödinger equation for a set of energies ϵ_k and are orthogonalized to the core states. Here the index i is a shorthand notation for the atomic site $\boldsymbol{R}_i$, the valence-electron quantum numbers $nlms$ and the reference energies ϵ_k used for the construction of the projectors. The index m stands for the band

index and the k-points within the first Brillouin zone. $|\tilde{\phi}_i\rangle$ are the pseudo-partial waves, which are functions of a radial grid multiplied by spherical harmonics, and coincide with the corresponding all-electron partial waves outside some augmentation region. Finally, the projector function $|\tilde{p}_i\rangle$ for each pseudo-partial wave is localized within the augmentation region and obeys the relation $\langle \tilde{p}_i|\tilde{\phi}_j\rangle = \delta_{ij}$. In this formalism, the charge density at a point r is the expectation value of the real-space projection operator $|r\rangle\langle r|$ and is given by

$$n(r) = \tilde{n}(r) + n^1(r) - \tilde{n}^1(r) \tag{2}$$

where the soft pseudo-charge density is

$$\tilde{n}(r) = \sum_m f_m \langle \tilde{\Psi}_m|r\rangle\langle r|\tilde{\Psi}_m\rangle \tag{3}$$

(f_m stands for the Fermi–Dirac occupation function). The on-site charge densities, n^1 and $\tilde{n}^1$, are expressed in terms of the projector functions and the pseudo-electron and all-electron partial waves:

$$n^1(r) = \sum_{m,(i,j)} f_m \langle \tilde{\Psi}_m|\tilde{p}_i\rangle\langle \phi_i|r\rangle\langle r|\phi_j\rangle\langle \tilde{p}_j|\tilde{\Psi}_m\rangle \tag{4}$$

and

$$\tilde{n}^1(r) = \sum_{m,(i,j)} f_m \langle \tilde{\Psi}_m|\tilde{p}_i\rangle\langle \tilde{\phi}_i|r\rangle\langle r|\tilde{\phi}_j\rangle\langle \tilde{p}_j|\tilde{\Psi}_m\rangle. \tag{5}$$

The total energy can be expressed as

$$E = \tilde{E} + E^1 - \tilde{E}^1 \tag{6}$$

where $\tilde{E}$, E^1 and $\tilde{E}^1$ are functions of the wavefunctions and the charge densities listed above. We refer the interested reader to the paper of Kresse and Joubert [18] for further theoretical details and now move on to discuss the details of our calculations.

2.2. Computational approach

Our calculations have used the Vienna *ab initio* simulation package VASP [18–22]. VASP is a first-principles plane-wave code which treats exchange and correlation in the local density approximation. In practice, the calculation may be performed using ultrasoft pseudopotentials [12, 13] or using the projector-augmented waves [17, 18]. Here the all-electron PAW method has been used. The solution of the Kohn–Sham equations is performed by using a matrix-diagonalization scheme based on a preconditioned band-by-band conjugate-gradient (CG) algorithm. Alternatively, for large systems, an efficient iterative matrix-diagonalization routine based on a sequential band-by-band residual minimization method of direct inversion in the iterative subspace (RMM–DIIS) is used. The charge density is updated using an improved Pulay mixing [23]. For the spin-polarized exchange and correlation potentials the GGA functional of Perdew *et al* [11] as implemented by White and Bird [24] is employed. The optimization of the atomic geometry, including the ionic coordinates, volume and shape of the unit cell, is performed via the conjugate-gradient minimization of the total energy, using the Hellmann–Feynman forces on the atoms and stresses on the unit cell.

Brillouin zone integrations in our calculations are performed on a grid of Monkhorst–Pack special points [25] using grids varying from $2 \times 2 \times 2$ to $4 \times 4 \times 4$ depending on the size of the unit cell. The linear tetrahedron method including Blöchl *et al* [26] corrections has been used for calculating the density of states and is rapidly convergent with respect to the k-point grid. The cut-off energy for the plane-wave expansion was fixed at 350 eV. The PAW formalism was used for all calculations.

3. Structural, electronic and magnetic properties

In the following we present our results for the structural electronic and magnetic properties of the sulphides of the 3d transition metals. Our investigations concentrated on two classes of compounds: (i) the monosulphides with the hexagonal NiAs structure and (ii) the disulphides with the pyrite (FeS_2-type) structure. In addition, we discuss the NaCl-type phase of MnS and investigate magnetic effects on the low-temperature structural phase transition of the NiAs-type monosulphides as an example of the transformation of FeS to the troilite phase. The crystal structures and measured lattice parameters of all compounds covered in this study are compared in table 1. Our results for the individual compounds are presented in a sequence corresponding to an increasing filling of the 3d band.

Table 1. The experimental crystal structures of the compounds considered in this study: lattice constants are given in Å.

	Structure	Bravais class	Space group	a	b	c
3d	VS(NiAs)	Hexagonal	$P6_3/mmc$ (194)	3.340	3.340	5.785
	CrS(NiAs)	Hexagonal	$P6_3/mmc$ (194)	3.439	3.439	5.324
	MnS(NaCl)	Cubic	$Fm\bar{3}m$ (225)	5.240	5.240	5.240
	MnS_2(FeS_2)	Cubic	$Pa\bar{3}$ (205)	6.091	6.091	6.091
	FeS(NiAs)	Hexagonal	$P6_3/mmc$ (194)	3.446	3.446	5.877
	FeS(troilite)	Hexagonal	$P\bar{6}2c$ (190)	5.958	5.958	11.740
	FeS_2(pyrite)	Cubic	$Pa\bar{3}$ (205)	5.428	5.428	5.428
	FeS_2(marcasite)	Orthorhombic	$Pnnm$ (58)	4.436	5.414	3.381
	CoS(NiAs)	Hexagonal	$P6_3/mmc$ (194)	3.370	3.370	5.528
	CoS_2(FeS_2)	Cubic	$Pa\bar{3}$ (205)	5.539	5.539	5.539
	NiS(NiAs)	Hexagonal	$P6_3/mmc$ (194)	3.439	3.439	5.324
	NiS_2(FeS_2)	Cubic	$Pa\bar{3}$ (205)	5.620	5.620	5.620

3.1. VS

The transition-metal chalcogenides, which have the NiAs-type crystal structure in the high-temperature range, have attracted much attention because of their magnetic ordering and structural transformations from the NiAs type to MnP type. VS shows a second-order structural phase transition from the NiAs type to the MnP type at about $T_T = 850$ K [27].

Previous electronic structure calculations for the NiAs phase of VS have been reported by Liu [28], Motizuki *et al* [27] and Raybaud *et al* [8]. The older calculations reported a high density of states at the Fermi level in the paramagnetic phase ($n(E_F) = 1.19$ states eV^{-1}/atom in reference [27], $n(E_F) = 1.30$ states eV^{-1}/atom in reference [28]) so, according to the Stoner–Wohlfahrt criteria, the paramagnetic state should be unstable with respect to the formation of an antiferromagnetic ground state. Raybaud *et al* [8] on the other hand report a density of states clearly below the threshold for the formation of a magnetically ordered phase ($n(E_F) \simeq 0.75$ states eV^{-1}/atom). According to Raybaud *et al* [8] the equilibrium atomic volume is strongly underestimated in the local density approximation ($V_{LDA}/V_{exp} = 0.89$), the use of the generalized-gradient approximation correcting for about half of the difference between theory and experiment ($V_{GGA}/V_{exp} = 0.95$). Our present PAW all-electron results are in good agreement with those obtained using ultrasoft pseudopotentials (but note that Raybaud *et al* have used the GGA only in the solid-state calculations, all pseudopotentials being constructed in the LDA only): $n(E_F) = 0.85$ states eV^{-1}/atom, $V_{PAW-GGA}/V_{exp} = 0.956$. The complete paramagnetic density of states is shown in figure 1. This good agreement
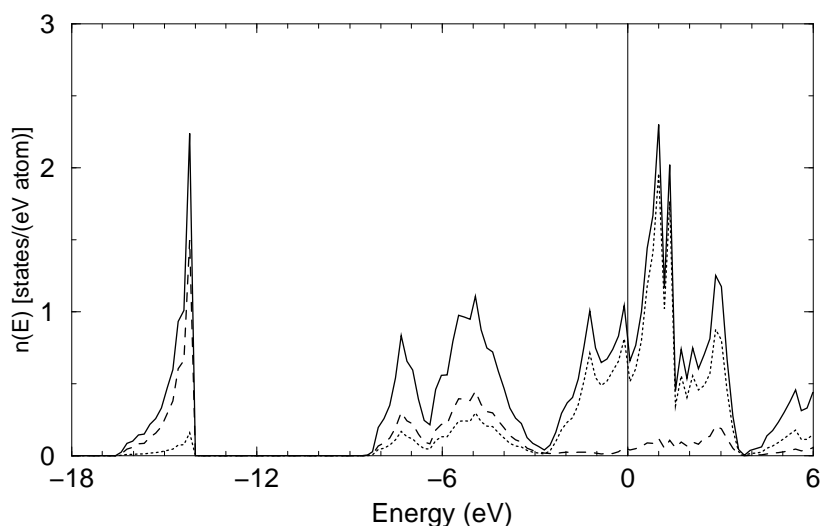
Figure 1. The density of states for VS. The metal and sulphur contributions are indicated by the dotted and dashed lines respectively.

between all-electron and pseudopotential calculations indicates that in this case the valence–core overlap is weak. We have also attempted to find an antiferromagnetic solution. However, irrespective of the values chosen for the initial moments, the calculations always converged to a non-magnetic solution.

A certain problem exists concerning the equilibrium axial ratio c/a of the hexagonal lattice. Ideal packing is achieved for $c/a = \sqrt{8/3}$, but among the more than fifty binary compounds crystallizing in the NiAs structure, c/a varies from $c/a \simeq 1.95$ for strongly ionic compounds (where the elongation of the unit cell is thought to be a consequence of the electrostatic repulsion of the TM cations which have their shortest distance along the c-axis) over nearly ideal values for semiconducting compounds to very small values ($c/a \geqslant 1.27$) for metallic compounds. Experimentally, $c/a = 1.73$ has been reported for VS. The value $c/a = 1.896$ resulting from the present all-electron calculations is slightly better than the pseudopotential result $c/a = 1.92$ of Raybaud *et al*, but still disturbingly at variance disagreement with experiment.

3.2. CrS

In the binary chromium selenides and sulphides, magnetic moments, mainly localized on Cr, are present. The exchange interactions are predominantly antiferromagnetic in these compounds [29, 30] in contrast to the ferromagnetic (FM) chromium tellurides. NiAs-type $Cr_{1-x}S$, which always has a few per cent Cr vacancies, exists only above 350 °C. When it is cooled below this temperature, a Jahn–Teller distortion around the Cr^{2+} (d^4) ions results in a monoclinic lattice [31]. High-temperature susceptibility data for above 900 K give the Curie–Weiss temperature $\Theta = -1585$ K and the effective paramagnetic moment has been estimated using molecular-field theory as $\mu_{eff} = 5.24 \ \mu_B$ [32].

Previous electronic structure calculations of Raybaud *et al* [8] predicted a high electronic density of states at the Fermi level for the structurally optimized paramagnetic phase ($n(E_F) \simeq 1.4$ states eV^{-1}/atom) and hence a tendency towards magnetic ordering. This is confirmed by the spin-polarized LDA results of Dijkstra *et al* [29] who found magnetic moments on the Cr

sites of ± 2.61 μ_B for the experimental structure. A remarkable fact is again that the GGA results, for the paramagnetic phase, in too small an equilibrium volume ($V_{GGA}/V_{exp} \simeq 0.93$) and too large a value for the axial ratio ($(c/a)_{GGA} = 1.82$, $(c/a)_{exp} = 1.55$). Our results for the paramagnetic phase agree well with those of Raybaud *et al*, demonstrating again the reliability of the pseudopotential approach for the paramagnetic phases. The spin-polarized calculations converge to an antiferromagnetic ground state with large moments of $\mu_{Cr} = \pm 2.545$ μ_B on the Cr sites. The magnetic energy difference is large, $\Delta E = 0.11$ eV/atom (see table 2; see also table 3); magnetism also leads to an expansion of the atomic volume by about 10%. The GGA atomic volume for the antiferromagnetic phase is now 3% larger than the experimental value. The formation of an antiferromagnetic ground state leads also to a substantial reduction of the axial ratio, from $c/a = 1.852$ for the non-magnetic phase to $c/a = 1.679$ for the antiferromagnetic state, which is, however, still apparently larger than the experimental value of $c/a = 1.548$ (cf. table 4).

Table 2. The experimental atomic volume, the ratio of measured to calculated volume, and the total energy in eV/atom for different magnetic states of transition-metal sulphides. The calculated ground state is given in bold lettering.

	Structure	V_{exp} (Å^3/atom)	V_{GGA}/V_{exp}	Energy (eV/atom)	Calculated magnetic type
3d	VS(NiAs)	13.97	0.956	**−7.408**	**NM**
	CrS(NiAs)	13.63	0.930	−7.158	NM
			1.034	**−7.268**	**AFM**
	MnS(NaCl)	17.99	0.718	−6.425	NM
			0.903	−6.964	FM
			0.933	**−6.992**	**Type-II AFM**
	MnS$_2$(FeS$_2$)	18.83	0.737	−6.102	NM
			0.927	−6.039	(HS) type-III AFM
			0.752	**−6.176**	**(LS) type-III AFM**
			0.747	−6.173	FM
	FeS(NiAs)	14.81	0.826	**−6.437**	**NM**
			0.952	−6.398	AFM
	FeS(troilite)	15.04	0.844	−6.456	NM
			0.891	**−6.475**	**AFM**
	FeS$_2$(pyrite)	13.33	0.992	**−6.002**	**NM**
	FeS$_2$(marcasite)	13.53	1.005	**−6.013**	**NM**
	CoS(NiAs)	12.69	0.985	**−5.848**	**NM**
	CoS$_2$(FeS$_2$)	14.16	0.972	−5.431	NM
			0.981	**−5.440**	**FM**
	NiS(NiAs)	13.63	0.986	**−5.083**	**NM**
	NiS$_2$(FeS$_2$)	14.79	0.999	**−4.821**	**NM**

All Cr ions are equivalent due to symmetry with the exception that spin-up and spin-down components are interchanged. The spin-polarized electronic density of states of AFM CrS is shown in figure 2. We find that CrS remains metallic although with a reduced density of states at the Fermi surface compared to the paramagnetic state. The s-dominated bands at higher binding energy are almost unchanged, but a pronounced exchange splitting appears in the Cr bands. The ratio of the exchange splitting, calculated in terms of the centre of gravity, $C_{\uparrow(\downarrow),l=2}^{Cr}$, of the Cr 3d bands to the magnetic moment may be used to estimate the Stoner parameter via the relations

$$\Delta E = C_{\uparrow,l}^{Cr} - C_{\downarrow,l}^{Cr} \tag{7}$$

Table 3. The magnetic ground state and magnetic moments. The bold lettering corresponds to the ground state found in our calculations.

	Structure	Experimental phase	Experimental magnetism (μ_B)	Reference	Calculated phase	Calculated magnetism (μ_B)
3d	VS(NiAs)	NM	0.0	[27]	**NM**	**0.0**
	CrS(NiAs)	AFM		[29]	**AFM**	**2.545**
	MnS(NaCl)	Type-II AFM	4.54	[34]	FM	3.966
					Type-II AFM	**4.082**
	MnS$_2$(FeS$_2$)	Type-III AFM		[46, 71, 72]	(HS) type-III AFM	3.827
					(LS) type-III AFM	**1.401**
					FM	1.163
	FeS(NiAs)	Paramagnetic	0.0	[48, 49]	**NM**	**0.0**
					AFM	2.675
	FeS(troilite)	AFM	4.0	[49, 54, 73]	**AFM**	**1.782**
	FeS$_2$(pyrite)	Diamagnetic	0.0	[61]	**NM**	**0.001**
	FeS$_2$(marcasite)	NM	0.0	[63]	**NM**	**0.0**
	CoS(NiAs)	Pauli paramagnetic	0.0	[54]	**NM**	**0.01**
	CoS$_2$(FeS$_2$)	FM	0.6–0.85	[59, 61, 66, 74]	**FM**	**0.762**
	NiS(NiAs)	AFM	1.6	[67, 75]	**NM**	**0.0**
	NiS$_2$(FeS$_2$)	AFM	1.17	[59, 61, 70]	**NM**	**0.015**

$$I = \frac{\Delta E}{\mu_{Cr}}. \tag{8}$$

We find a value of $I = 0.914$ eV μ_B^{-1} which is in reasonable agreement with the value 0.95 ± 0.015 eV μ_B^{-1} found for a large number of 3d-band intermetallic compounds. A value of the Stoner parameter close to 1 eV μ_B^{-1} is characteristic for itinerant band magnetism [33].

3.3. MnS

Under ordinary conditions MnS has the rock-salt structure (α-MnS). Below its spin-freezing (Néel) temperature (75–150 K), α-MnS is stable with the antiferromagnetic spin-ordered type-II structure in which the individual atomic moments are aligned in $\langle 111 \rangle$ ferromagnetic sheets with adjacent sheets having anti-parallel spins. Experimentally, Mn moments of $\mu = 4.54 \, \mu_B$ [34] have been reported. Sato *et al* [35] have recently investigated this material using ultraviolet photoemission and inverse-photoemission spectroscopy. Their results indicate that bonding states derive from the hybridization between Mn 3d and S p orbitals. The energy separation between the valence-band maximum and the conduction-band minimum is 2.7 eV, in agreement with the position of the optical absorption edge [36].

For MnS, the non-spin-polarized calculations of Raybaud *et al* [8] led to the largest disagreement of the calculated equilibrium atomic volume with experiment—even with the GGA the calculation underestimates the volume by as much as 27%. Due to the simplicity of the crystal structure, the magnetic structure of MnS has been studied repeatedly using various band-structure techniques: Wei and Zunger [37] used the linearized-augmented-plane-wave method in combination with the LSDA to investigate all three Mn monochalcogenides. For MnTe an antiferromagnetic type-II ground state with magnetic moments of $\mu_{Mn} = \pm 4.38 \, \mu_B$ is predicted. Results for MnS are given only including an empirical correction to the d-band potential, resulting in the same antiferromagnetic ordering and moments of $\mu_{Mn} = \pm 4.34 \, \mu_B$ (all results referring to the experimental lattice constant). Hines *et al* [38] reported periodic

Table 4. The atomic volume (in $Å^3$/atom) and structural parameters. The bold lettering corresponds to the ground state found in our calculations. For the troilite phase the maximum displacement of ions from the ideal NiAs positions is indicated by d.

	Structure	V_{exp}	c/a ratio$_{exp}$		V_{GGA}	Bravais class	c/a ratio$_{calc}$		Calculated phase
3d	VS(NiAs)	13.97	1.732		13.338	Hexagonal	**1.896**		**NM**
	CrS(NiAs)	13.63	1.548		12.683	Hexagonal	1.852		NM
					14.098	Hexagonal	**1.679**		**AFM**
	FeS(NiAs)	14.81	1.673		12.233	Hexagonal	**1.525**		**NM**
					14.098	Hexagonal	1.677		AFM
	CoS(NiAs)	12.69	1.640		12.498	Hexagonal	**1.530**		**NM**
	NiS(NiAs)	13.63	1.548		13.443	Hexagonal	**1.499**		**NM**

	Structure	V_{exp}			V_{GGA}	Bravais class	u_{exp}	u_{calc}	Calculated phase
3d	MnS_2(FeS_2)	18.83			13.887	Cubic	0.091	0.125	NM
					17.510	Cubic		0.102	(HS) type-III AFM
					14.155	Cubic		**0.120**	**(LS) type-III AFM**
					14.058	Cubic		0.121	FM
	FeS_2(pyrite)	13.33			13.219	Cubic	0.115	**0.117**	**NM**
	CoS_2(FeS_2)	14.16			13.764	Cubic	0.110	0.116	NM
					13.895	Cubic		**0.113**	**FM**
	NiS_2(FeS_2)	14.79			14.858	Cubic	0.106	**0.107**	**NM**

	Structure	V_{exp}			V_{GGA}	Bravais class			Calculated phase
3d	MnSp(NaCl)	17.99			12.915	Cubic			NM
					16.788	Cubic			**Type-II AFM**

	Structure	V_{exp}	c/a ratio$_{exp}$	d_{exp} (Å)	V_{GGA}	Bravais class	c/a ratio$_{calc}$	d_{calc} (Å)	Calculated phase
3d	FeS(troilite)	15.04	1.967	0.2950	12.695	Hexagonal	1.796	0.4102	NM
					13.385	Hexagonal	**1.831**	0.3785	**AFM**

	Structure	V_{exp}	c/a ratio$_{exp}$		V_{GGA}	Bravais class	c/a ratio$_{calc}$		Calculated magnetic type
3d	FeS_2(marcasite)	13.53	1.601		13.597	Orthorhombic	**1.596**		**NM**

Hartree–Fock calculations using the CRYSTAL code [39]. The magnetic ground state is described as an antiferromagnetic type-II state with moments of $\mu_{Mn} = 4.89\ \mu_B$ at the experimental lattice constant and $\mu_{Mn} = 4.92\ \mu_B$ at the lattice constant optimized for the ferromagnetic phase of MnS. This is virtually identical to the Hund's-rule limit of 5 μ_B. The optimized lattice constant corresponds to an overestimate of the equilibrium volume by about 12%, which is reduced to 0.5% by including correlation corrections. No equilibration of the lattice constants has been performed for the antiferromagnetic phase, assuming (as we shall see, incorrectly) that the magneto-volume effect remains the same, independently of the type of magnetic ordering. An extremely large exchange splitting has been reported, placing the filled Mn 3d spin-up band at about −8 eV below the Fermi level (and also below the S 3p band) and the bottom of the empty Mn 3d spin-down band at +11 eV.

Very recently Tappero *et al* [40, 41] reported calculations using CRYSTAL with *a posteriori* corrections to the Hartree–Fock energy calculated using different variants of
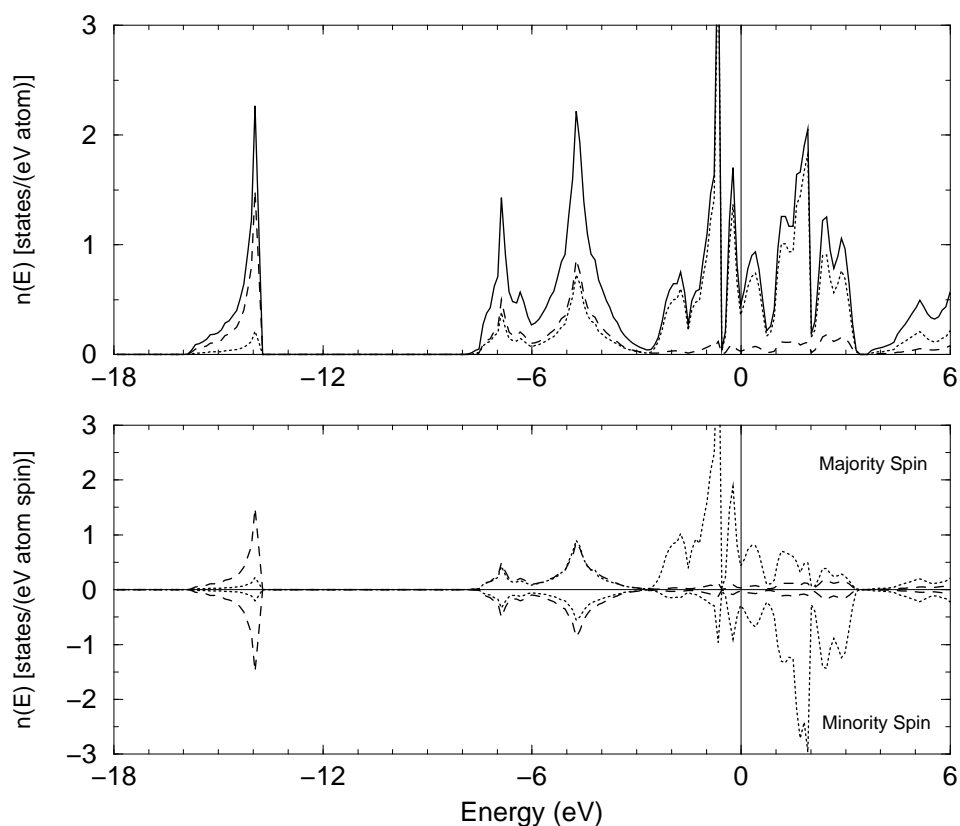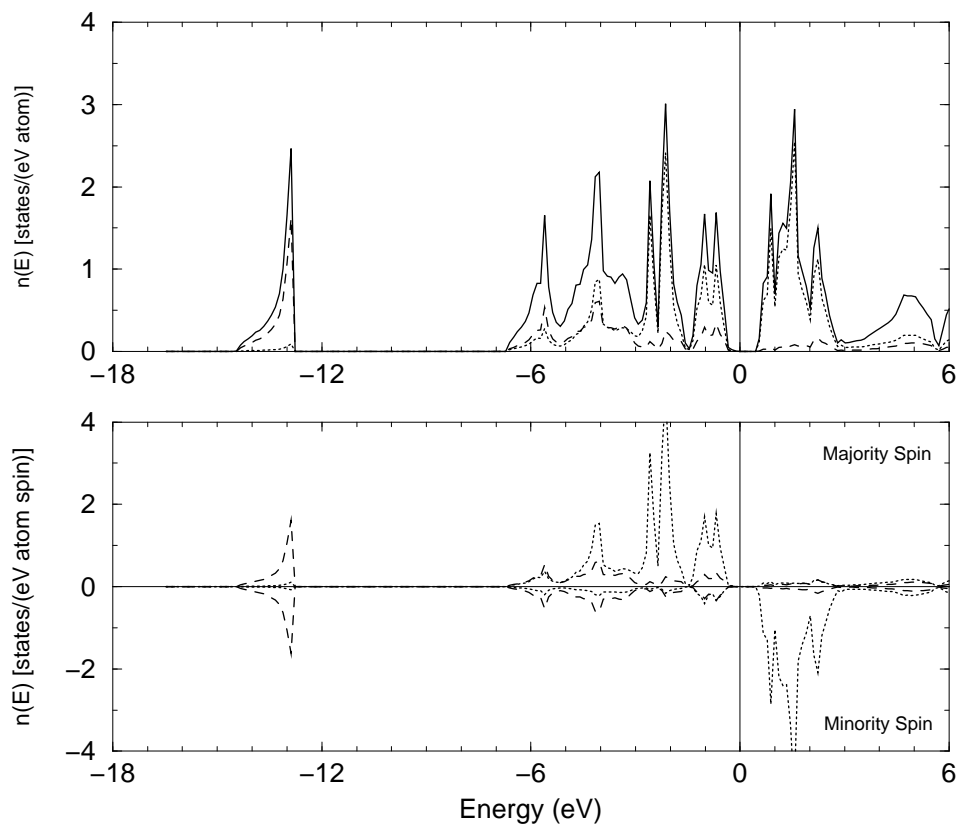
Figure 2. Spin-polarized total and partial densities of states for antiferromagnetic CrS. The metal and sulphur contributions are indicated by the dotted and dashed lines respectively. The upper figure shows the total density of states. Majority- and minority-spin contributions are separated in the lower figure.

the LSDA and GGA. The volume has been optimized independently for the ferromagnetic and antiferromagnetic type-II phases. For the Hartree–Fock approximation, the equilibrium atomic volume is overestimated by about 15% in both magnetic phases, thus confirming a small difference in the magneto-volume effects in the Hartree–Fock approximation. The overestimate is reduced to about 2.5% by correlation corrections at the GGA level. The correlation corrections are also shown to have a dramatic effect on the electronic properties; the Hartree–Fock gap of about 11 eV is reduced to 1.5 eV (this is the value quoted by the authors in the text, their figures showing a non-vanishing density of states at E_F and a gap only within the valence band—hence antiferromagnetic MnS would be metallic). The Mn magnetic moment, however, is only little affected, and reduced from 4.9 μ_B in the Hartree–Fock case to about 4.6 μ_B with correlation corrections.

In our calculations we have considered the paramagnetic, antiferromagnetic type-II and ferromagnetic phases of MnS. Both the ferromagnetic and antiferromagnetic type-II phases are lower in energy than the non-magnetic phase by about 0.55 eV/atom. The magnetic ordering causes an increase of the atomic volume by about 30% (see table 2 for details). In contrast to the Hartree–Fock predictions, the magneto-volume effect is distinctly larger for the antiferromagnetic type-II phase than for the ferromagnetic phase. However, even for the

antiferromagnetic type-II phase, the equilibrium atomic volume of MnS is still underestimated by about 6.7%. The computed magnetic moment is $\mu_{Mn} = 3.97\,\mu_B$ in the ferromagnetic phase and $\mu_{Mn} = \pm 4.08\,\mu_B$ in the antiferromagnetic case, in good agreement with the experimental value of $\mu_{Mn} = 4.54\,\mu_B$ (reference [34]), but distinctly lower than the values derived from the Hartree–Fock and correlation-corrected Hartree–Fock calculations. This difference is also reflected in the electronic structure shown in figure 3. The site-projected density of states demonstrates a strong Mn 3d–S 3p hybridization in the lower part of the valence band (which is only slightly affected by the exchange splitting). This hybridization is responsible for the lowering of the Mn moments below the Hund's-rule limit. In the Hartree–Fock limit there is no Mn–S hybridization, the majority- and minority-spin Mn d bands lying on either side of the S 3p band. The correlation corrections induce huge shifts of all bands and lead again to a strong Mn–S hybridization. Our calculations predict a gap of $\sim$1 eV separating the top of the Mn 3d majority band from the bottom of the Mn 3d minority band. This is of the same order of magnitude as reported for the correlation-corrected Hartree–Fock calculations [40, 41] (see our remarks above), and substantially lower than the gap of 2.7 eV measured in the photoemission (PES), inverse-photoemission (IPES) and optical absorption measurements. Comparison with the density of states of the paramagnetic phase (see Raybaud *et al* [8]) shows that the antiferromagnetic ordering leads to an occupation of antibonding d states for


Figure 3. The spin-polarized density of states for MnS. The metal and sulphur contributions are indicated by the dotted and dashed lines respectively. The upper figure shows the total density of states. Majority- and minority-spin contributions are separated in the lower figure.

the majority spins and a depletion of bonding d states for the minority spins, leading to the large calculated (and observed) magneto-volume effect. Estimating the exchange splitting as described above for CrS, we derive a Stoner parameter of $I \sim 0.91$ eV μ_B^{-1} in accordance with an itinerant character of the magnetism in MnS. Sato *et al* [35] derived from the positions of the peaks in the PES and IPES spectra an exchange splitting of 8.0 ± 0.2 eV. Applying the same procedure and allowing for a finite experimental resolution which tends to smear out the double peaks in the d bands, we find an exchange splitting of 4.2 eV.

The underestimation of the gap width, and in this case also of the exchange splitting, is a characteristic property of density-functional theory. The underestimation of the gap (1 eV versus 2.7 eV) is of the same order as for other narrow-gap semiconductors. Discrepancies in the calculated and measured exchange splitting have also been found in the homologous and iso-structural compound MnO. For Mn monoxide it has been shown that the strong intra-atomic correlation due to the Coulomb repulsion in the narrow Mn d band is substantially underestimated in a local spin-density approximation. An improved description of this intra-atomic correlation may be based on the LDA + U method [2, 42] in which a Hubbard-like on-site interaction U is added to the LDA Hamiltonian. Treating U as an adjustable parameter, it is found that a value of $U \sim 10$ eV is necessary to account for the experimentally observed exchange splitting in MnO [42, 43]. Preliminary results [44] also show that the LDA + U approach also leads to a more accurate description of the exchange splitting and of the semiconducting gap in MnS, albeit with a considerably smaller value for the on-site interaction than in MnO.

3.4. MnS$_2$

MnS$_2$ crystallizes in the cubic pyrite structure above the Néel point, with space group $Pa3$, and consists of an NaCl-like arrangement of Mn^{2+} and $(S_2)^{2-}$ ions, with the axes of the $(S_2)^{2-}$ groups directed along the various body diagonals of the cell. The atomic positions of the Mn atoms are 4a $(0, 0, 0)$, S atoms occupying positions 8c (u, u, u). Compared to the other pyrite-type disulphides, MnS$_2$ has an exceptionally low value of $u = 0.099$, leading also to a short bond length of the S–S pairs. The magnetic structure is collinear, consisting of an antiferromagnetic ordering of the 'third' kind. It is described by a propagation vector $\mathbf{k} = (2\pi/a)(\frac{1}{2}, 0, 1)$, where a is the lattice constant. The magnetic unit cell is thus doubled along the x-axis. Planes perpendicular to this axis are individually antiferromagnetic and alternate with a period equal to the chemical cell length. See figure 4 for details.
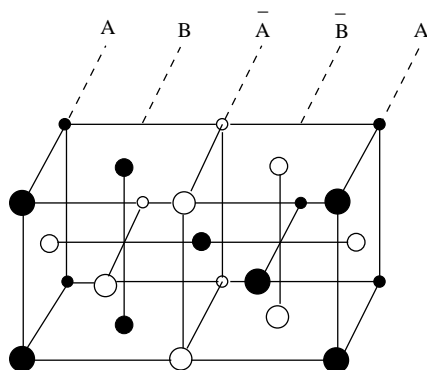

Figure 4. The type-III single-$\mathbf{k}$ antiferromagnetic structure of MnS$_2$. The solid and open circles represent atoms with oppositely directed spin orientations. The sulphur atoms have been omitted.

The antiferromagnetic phase transition at $T_N = 48.2$ K is found to be first order [45]. Chattopadhyay *et al* [46] have found that MnS_2 behaves as a Mott insulator between T_N and 100 K. Additionally, Chattopadhyay *et al* [47] have used neutron diffraction to examine single crystals of MnS_2 and observed that the crystal consists of magnetic domains with spin directions oriented equally along the three crystallographic directions.

Our calculations indicate that the non-magnetic phase of MnS_2 is metallic and has an equilibrium atomic volume that is about 25% smaller than the experimental value. A ferromagnetic phase with a magnetic moment of $\mu_{Mn} = 1.16$ μ_B and a low-spin anti-ferromagnetic type-III phase with moments $\mu_{Mn} = \pm 1.40$ μ_B are about 73 meV/atom lower in energy than the non-magnetic phase, the antiferromagnetic phase being more favourable than the ferromagnetic phase by only 3 meV/atom. In both magnetic phases the equilibrium volume is only slightly expanded over the non-magnetic case (see table 2 and figure 5(a)), and the structural parameter u is only slightly reduced compared to the non-magnetic value. At expanded volumes, however, the antiferromagnetic phase undergoes a low-spin/high-spin transition coupled to a structural phase transition resulting in a discontinuous reduction of the structural parameter u and a similar decrease of the S–S bond length by about 15%. The equilibrium atomic volume of the high-spin antiferromagnetic phase is 17.51 Å^3, in much better agreement with the experimental value of 18.83 Å^3 than any of the low-spin or non-magnetic phases. At this metastable equilibrium, the manganese magnetic moment is calculated to be $\mu_{Mn} = 3.83$ μ_B. Note that a low-spin/high-spin transition also occurs in the ferromagnetic phase at approximately the same volume. Figure 5 summarizes the variation of energy, structure and magnetic moments with volume in all three phases. The type-III antiferromagnetic ordering also breaks the cubic symmetry of the pyrite cell, but the orthorhombic distortions determined by a full re-optimization remain small: b/a deviates from unity by 0.34% in the high-spin phase and by 0.02% in the low-spin phase, the variation of the c/a ratio being comparably small in the two phases. However, the energy of the high-spin antiferromagnetic phase is even higher than that of the non-magnetic phase.

Figure 6 illustrates our results for the electronic structure. Whereas the non-magnetic phase is metallic, with the Fermi level falling close to the upper edge of the Mn t_{2g} band and separated by a substantial pseudogap from the Mn e_g band, all magnetic phases are found to be semi-metallic. For both the ferromagnetic and the low-spin antiferromagnetic phases, the t_{2g} band of the majority spins is completely filled and a narrow pseudogap is found in the t_{2g} band of the minority spins. Note that the t_{2g} orbitals are oriented perpendicular to the Mn–S bonds; hence they are essentially non-bonding. The e_g orbitals extend along the Mn–S bonds and hybridize strongly with the S 3p states. A broad band just below the Mn t_{2g} bands is formed by S pσ, pπ and p$\pi^\star$ states and Mn bands, while for the non-magnetic and low-spin phases, the Mn e_g + S p$\sigma^\star$ band remains empty. The total density of states is nearly zero at E_F in all three phases.

In the high-spin antiferromagnetic phase, the electronic structure is very different: the shorter S–S bond length increases the S sσ/S s$\sigma^\star$ and S pσ/S p$\sigma^\star$ bonding/antibonding splitting and leads to a decreased Mn e_g–S 3p hybridization. For the majority spins both the t_{2g} and the e_g bands are occupied; for the minority spins they are empty. The Fermi level falls into a very narrow band-gap. Due to some remaining Mn–S hybridization, the Mn moment is reduced below the Hund's-rule limit of 5 μ_B. The change in the electronic structure in going from the low-spin to the high-spin antiferromagnetic phase is also important for the chemical properties of MnS_2 due to the change of the frontier orbitals from t_{2g} to e_g character—hence the antiferromagnetic semi-metal MnS_2 will have completely different catalytic properties to the iso-structural non-magnetic FeS_2 and RuS_2 compounds (we refer the reader to the discussion in Raybaud *et al* [7, 8]).
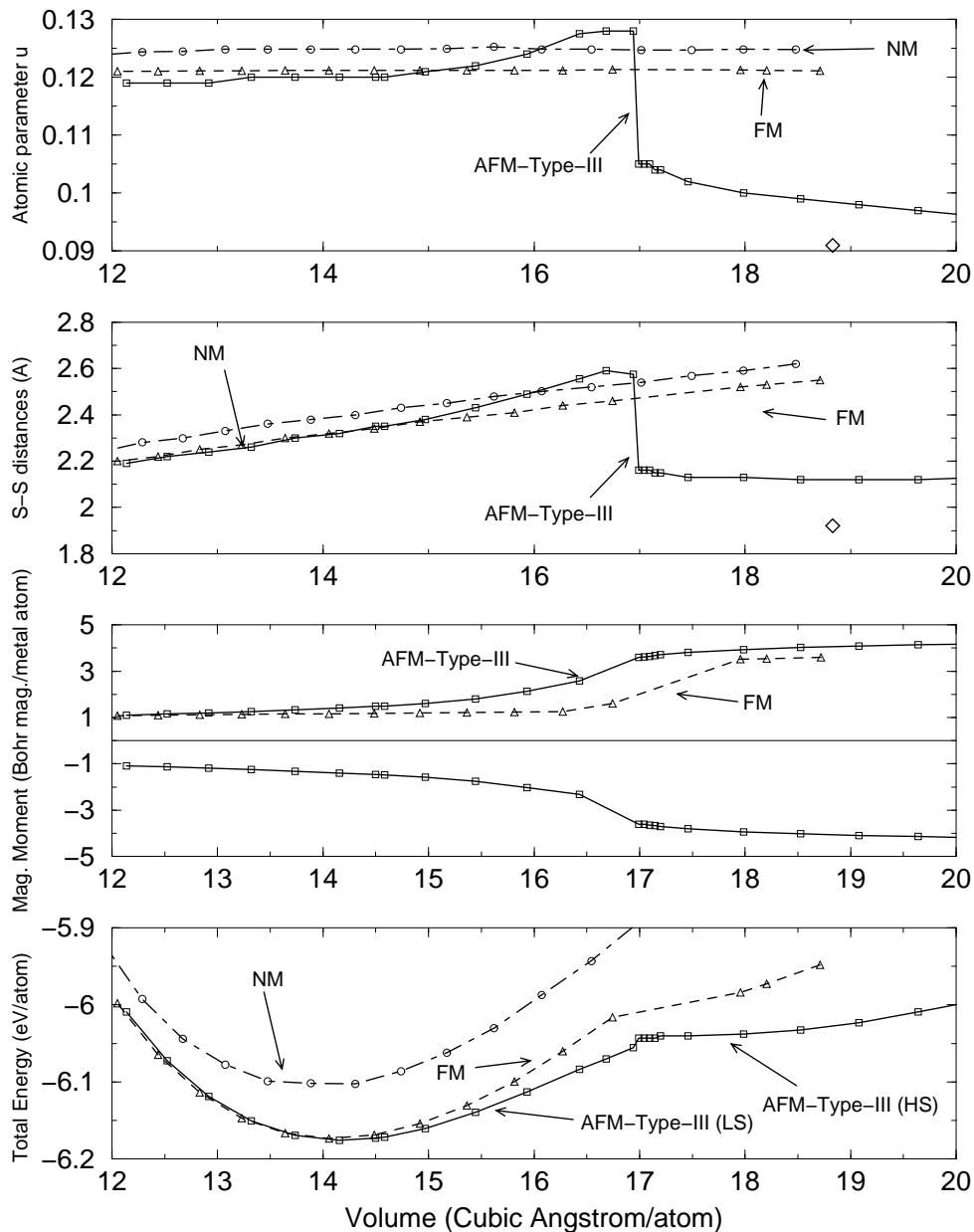
Figure 5. Total energy plotted against volume for MnS$_2$ in the non-magnetic (NM), ferromagnetic (FM) and antiferromagnetic (AFM) type-III states (high- and low-spin solutions). Also shown are the calculated magnetic moments, the S–S distances and the structure parameter u as functions of volume. The experimental data, when available, are indicated by diamonds.

The remaining problem is the large energy difference between high-spin/high-volume and low-spin/low-volume states. Evidently the problem is closely related to the underestimate of the semiconducting gap and of the exchange splitting in the monosulphides (see the preceding section). However, due to the lower d bandwidths in the disulphides, correlation effects are
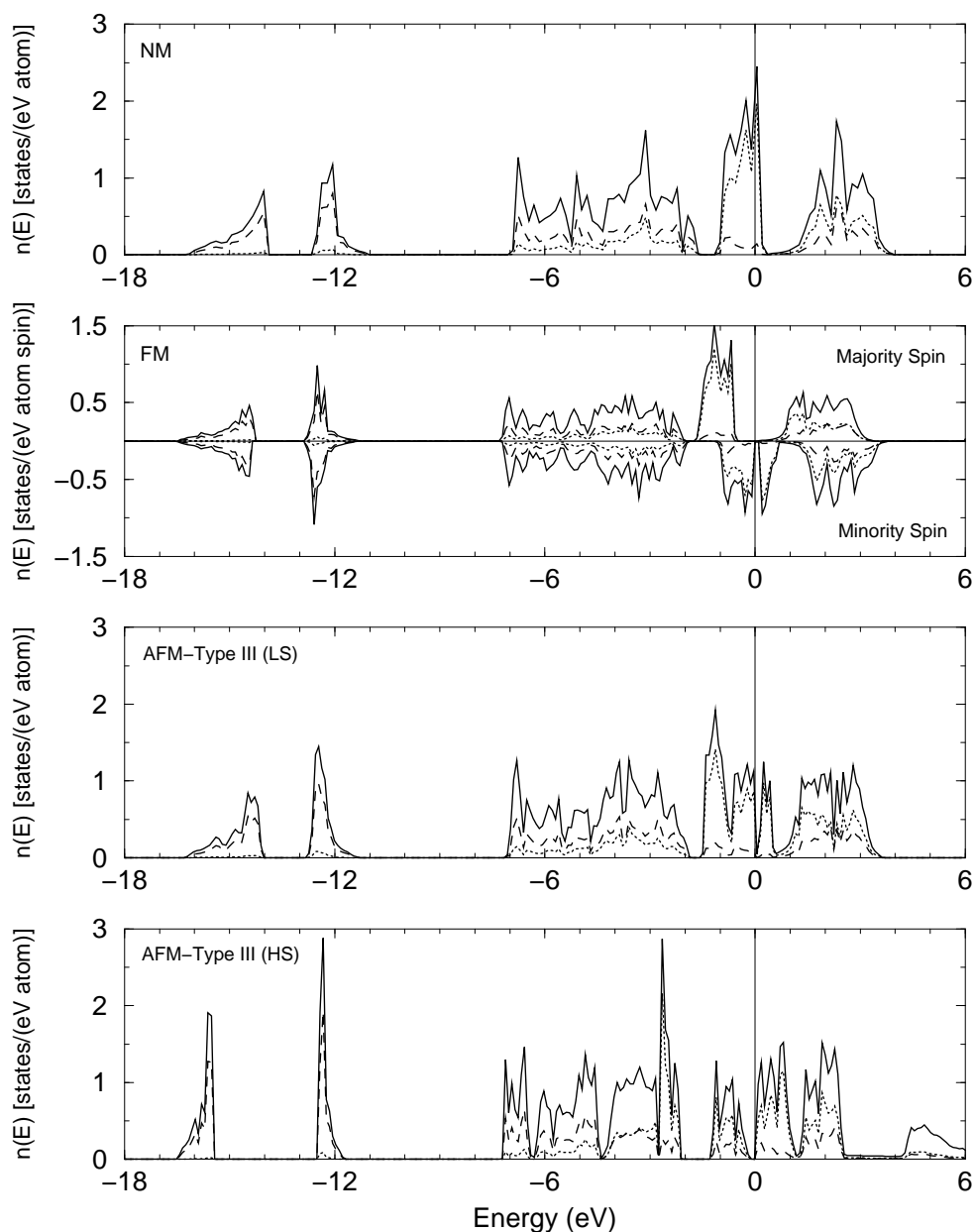
Figure 6. Densities of states, for non-magnetic (NM), ferromagnetic (FM) and both low-spin (LS) and high-spin (HS) type-III antiferromagnetic (AFM) MnS_2. The format is the same as in the earlier plots of densities of states. For the FM phase the spin-polarized density of states is shown. See figure 7 for the spin-polarized density of states of the AFM phase.

expected to play an even more important role for the stabilization of the high-spin state in this material. We expect the calculated band-structure and magnetic moments to be quite realistic, except for the absence of the real band-gap. Electron spectroscopy and optical measurements which are suitable for testing this conjecture would be very valuable.
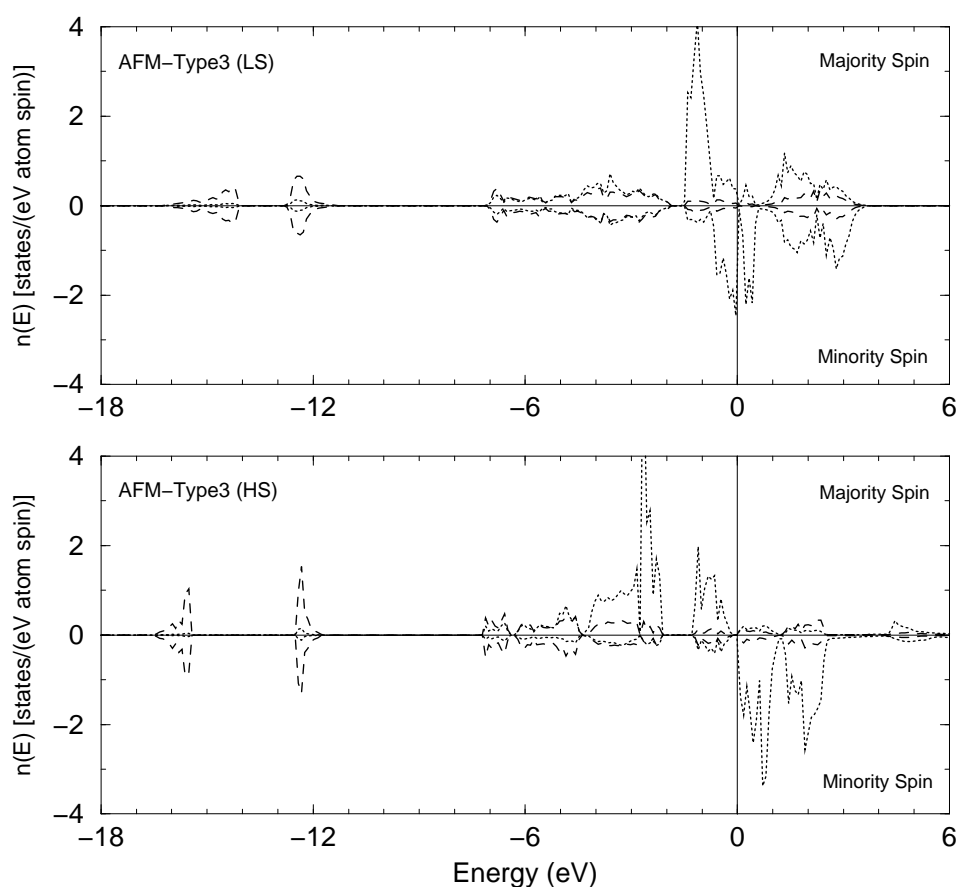
Figure 7. Spin-polarized densities of states for LS and HS type-III antiferromagnetic MnS_2. The figures show the contributions from one Mn (dotted line) and one S (dashed line) ion.

3.5. FeS, NiAs versus troilite structure

FeS(troilite) has been investigated extensively because natural troilite can be found in meteorites and is an important material in Earth and space sciences. Additionally, iron sulphides including troilite show a variety of magnetic properties and crystal structures. FeS is antiferromagnetic below the Néel temperature of $T_N = 593$–598 K. Above $T_\alpha = 420$ K, FeS is commonly reported to be a metal with the NiAs-type crystal structure. However, King and Prewitt [48] found that this conclusion is inconsistent with the experimental data and have shown that two structural phase transitions occur as the temperature is raised. They found that below 420 K and ambient pressure, FeS is an insulator with a narrow band-gap of 0.04 eV. This is known as the α-transition, and is accompanied by a small displacement of the Fe and S atoms from the regular NiAs structure leading to the troilite structure. As the temperature rises, FeS transforms at 420 K and ambient pressure, and at 298 K and 3.4 GPa, to an MnP-type structure. This structure has space group $Pnma$ and the orthohexagonal unit-cell dimensions $a = C$, $b = A$ and $c = \sqrt{3}A$ [48]. Further increases in temperature, above 600 K at ambient pressure, produce a second-order transition to an NiAs structure. As FeS is known to be paramagnetic above 600 K [49] this necessarily implies that FeS(NiAs) is paramagnetic.

The existence of two-temperature and pressure-induced phase transitions (troilite $\rightarrow$ MnP type $\rightarrow$ NiAs type) and the stabilization of the MnP and NiAs phases under increased pressure were also confirmed by extended x-ray diffraction studies of Kusaba *et al* [50,51]. The electronic and magnetic properties of FeS were investigated by Coey and Roux-Buisson [49] using x-ray diffraction and Mössbauer spectroscopy. The antiferromagnetic troilite phase was characterized as a high-spin localized-moment phase with $\mu_{Fe} \simeq 4 \mu_B$. Shimada *et al* [52] have performed spin-integrated and spin-resolved photoemission and inverse-photoemission studies, confirming the localized nature of the Fe 3d states. The photoemission study suggests a very low density of states at the Fermi level, and this is confirmed by electronic specific heat measurements by Kobayashi *et al* [53]. Spin-polarized electronic structure calculations for FeS in the NiAs phase have been performed by Ikeda *et al* [54]. These calculations have also been extended to Fe_7S_8 (pyrrhotite) which forms a superstructure of the NiAs lattice with ordered Fe vacancies [55]. Calculations for the homologous selenides have been reported by Ikeda *et al* [56]. Compared to the experimental spectra, the local spin-density calculations show an increased density of states at the Fermi level and a less pronounced exchange splitting. For NiAs-type FeS, Ikeda *et al* [54] quote an antiferromagnetic moment of $\pm 3 \mu_B$ at the experimental volume but no information is given on whether the non-magnetic or the antiferromagnetic state is more stable. For pyrrhotite (Fe_7S_8), Shirai *et al* [55] report a ferrimagnetic structure with Fe moments of 3.2, 2.9 and $-3.0 \mu_B$. Almost the same moments have been reported for Fe_7Se_8. So far no attempt has been made to calculate the structural energy and volume differences in the competing FeS phases.

In our present work we have considered the non-magnetic and antiferromagnetic phases of FeS in the NiAs and troilite structures. The results for the structure and magnetic moments are shown in figure 8. For NiAs-type FeS we find a non-magnetic ground state with a very low equilibrium volume which is about 17% lower than the experimental equilibrium volume. The non-magnetic ground state is also confirmed by recent full-potential augmented-plane-wave calculations of Sherman [57]. An antiferromagnetic solution exists only at a substantially expanded volume, the structural energy difference being 30 meV/atom. The NM $\rightarrow$ AFM transition is first order and accompanied by a structural transformation, with a substantial increase of the axial ratio of the hexagonal cell (where the antiferromagnetic value agrees better with experiment). At the metastable equilibrium volume the Fe magnetic moment is about $2.7 \mu_B$, in agreement with the value reported by Ikeda *et al* [54].

At atomic volumes smaller than about 12 Å^3/atom, the troilite phase is energetically almost degenerate with the NiAs phase (but not structurally identical). At these densities, troilite is non-magnetic. For larger volumes, the antiferromagnetic state is stabilized, but the onset of magnetic ordering is not discontinuous as in the NiAs phase—the magnetic moment develops rather slowly on expansion. An increasing magnetic polarization is also accompanied by a change in the crystal structure as in the NiAs phase. Antiferromagnetic troilite has a larger axial ratio than the non-magnetic state but still substantially smaller than the experimental value; cf. table 4. Interestingly, we find that the deviation of the atomic positions in troilite from the high-symmetry locations in the NiAs phase is smaller in the antiferromagnetic than in the non-magnetic state (see figure 8). Nevertheless, this deviation results in an exaggerated distortion of the crystal structure. Of the three symmetrically distinct S atoms, only S(2) is significantly displaced along the *c*-axis, resulting in the formation of Fe prisms which are capped by S(2) atoms. The Fe atoms are drawn into this triangular group and also out from the centre of the surrounding octahedron. Altogether, our antiferromagnetic relaxation results in ionic displacements 5–6% larger than expected. The magnetic moment of antiferromagnetic troilite at equilibrium is calculated to be $\mu_{Fe} = \pm 1.78 \mu_B$. This is considerably lower than the high-spin value of $4 \mu_B$ reported by Coey and Roux-Buisson [49] and also lower than
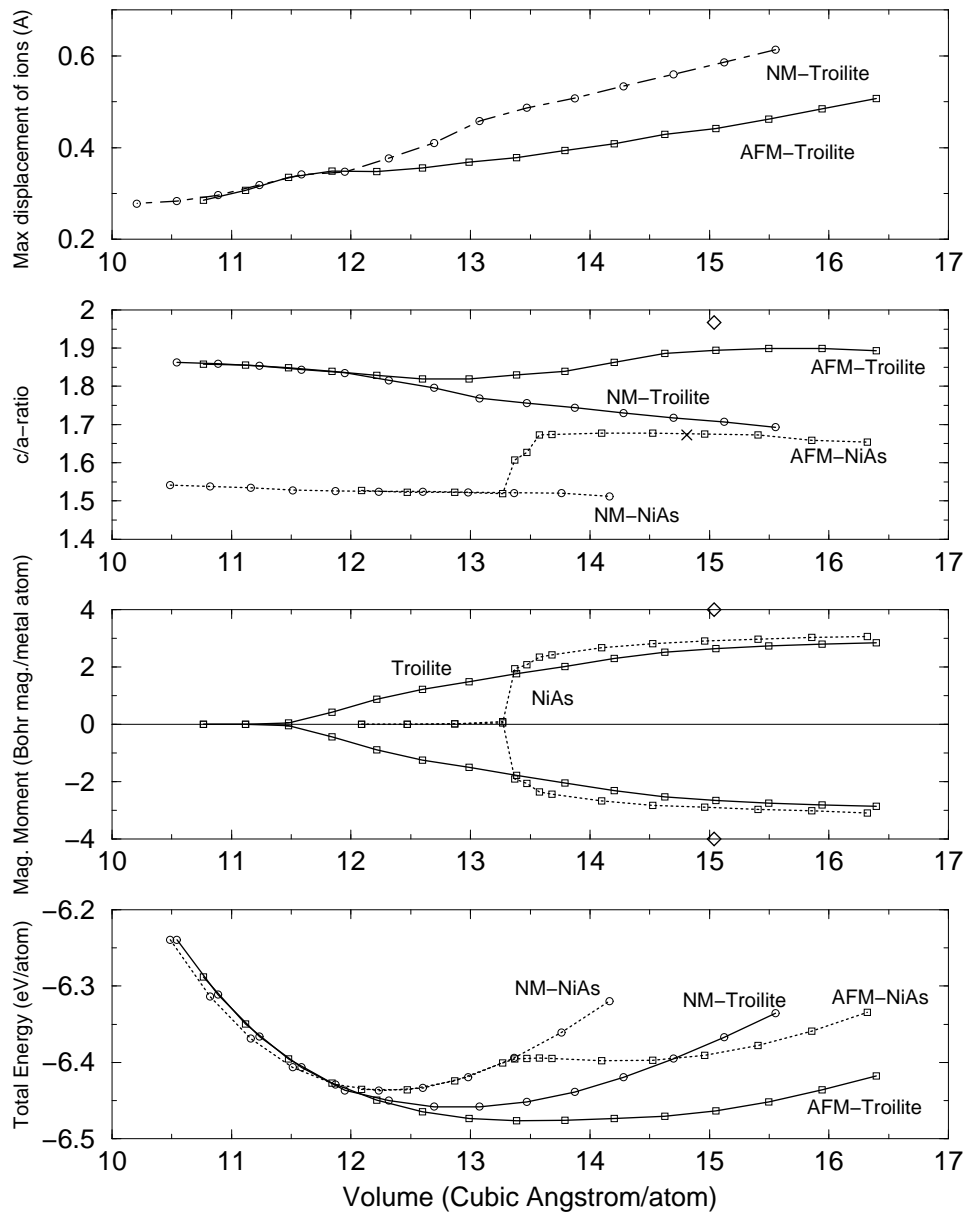
Figure 8. Total energy plotted against volume for FeS in the non-magnetic and ferromagnetic NiAs-type and troilite phases. Also shown are the calculated magnetic moments, the c/a ratio and the maximum displacement of the ions in troilite from their positions in the ideal NiAs structure as functions of volume. A cross indicates experimental data for the NiAs-type structure while a diamond indicates experimental data for the troilite structure.

the value that we have obtained for the metastable antiferromagnetic NiAs phase; cf. also table 3. The energy-versus-volume curves of the NiAs and troilite phases intersect at a volume slightly lower than 12 Å^3/atom, predicting a pressure-induced structural phase transition at a volume reduction of about $\Delta V/V \sim 13\%$ in good agreement with the observations by x-ray

diffraction [50, 51] and Mössbauer spectroscopy [53]. However, our calculations suggest that at the pressure where the phase transition occurs, the magnetic moment of troilite is already quite small ($\mu_{Fe} \sim 0.9\ \mu_B$), whereas experiment [53] suggests a more considerable magnetic discontinuity.

The electronic spectra of the non-magnetic NiAs phase and antiferromagnetic troilite are reported in figure 9. The results reported for NiAs-type FeS are in very good agreement with those of Raybaud *et al* [8] and Ikeda *et al* [54]. For troilite we find a considerably more spiky density of states—which is a direct consequence of the lower crystalline symmetry. In the paramagnetic troilite phase, the density of states at E_F is reduced compared to that in the NiAs phase and this leads also to a reduced exchange splitting and a stronger S 3p–Fe 3d overlap— a direct consequence being the reduced antiferromagnetic moment. In antiferromagnetic troilite, we calculate a substantial density of states of the minority spins at the Fermi level, in contradiction to the very low density of states inferred from the PES and IPES spectra of Shimada *et al* [52] and to the zero density of states derived from the electronic specific heat measurements.

Figure 10 shows a comparison of the calculated and measured photoemission and inverse-photoemission spectra (theoretical spectra are obtained by weighting the calculated partial density of states with the corresponding photoemission cross-sections—for FeS, the spectra are strongly dominated by the Fe 3d contributions). Theory and experiment differ not only in the density of states at E_F, but in addition in the structure close to E_F: the peak in the unoccupied band at about +0.5 eV and the shoulder in the occupied band at −0.3 eV arise from the high minority density of states. The peaks between −1 and −2 eV arise from the majority density of states and should be shifted to higher binding energies. All of this indicates that the exchange splitting is underestimated. However, it has to be emphasized that our troilite spectra agree better with experiment than the antiferromagnetic NiAs results of Shimada *et al* [52].

All of the remaining discrepancies between theory and experiment—(i) absence of a semiconducting gap, too-small exchange splitting, (ii) too-low magnetic moment and (iii) too-small equilibrium volume—suggest that correlation effects are important in FeS. Cluster-model configuration-interaction (CI) calculations performed by Shimada *et al* [52] suggest a d–d on-site Coulomb interaction of $U \sim 5$ eV—this would place FeS, like MnS, in the regime intermediate between itinerant and strongly correlated systems. However, the agreement of the model CI calculations with experiment is not satisfactory. LDA + U calculations seem to offer an attractive alternative.

3.6. FeS$_2$, pyrite and marcasite

The magnetic properties of FeS$_2$ (pyrite) are unusual. Fe appears to have no magnetic moment in this material. Gorter and Wojtowicz [58] found that FeS$_2$ showed a weak, temperature-independent paramagnetic susceptibility, measured by means of a magnetic balance. Additionally FeS$_2$ is a semiconductor, as confirmed by the photoemission and inverse-photoemission data of Fujimori *et al* [59] and of Folkerts *et al* [60]. This picture is confirmed by detailed band-structure calculations [8, 61].

The semiconducting character of FeS$_2$ was first explained by Néel and Benoit [62] as follows: sixteen valence electrons, of which eight come from Fe and eight from S$_2$, are redistributed in the FeS$_2$ molecule such that the covalent Fe–S and S–S bonds are saturated, ten electrons occupying perfectly the 3d shell of Fe, and six the 3p shell of S.

In FeS$_2$, the metal 3d e$_g$ levels are unoccupied and mix strongly with the antibonding S 3pσ^* states. The compound is a semiconductor with an indirect band-gap between the Fe 3d t$_{2g}$ and e$_g$ states. The predicted band-structure is in good agreement with the PES and IPES
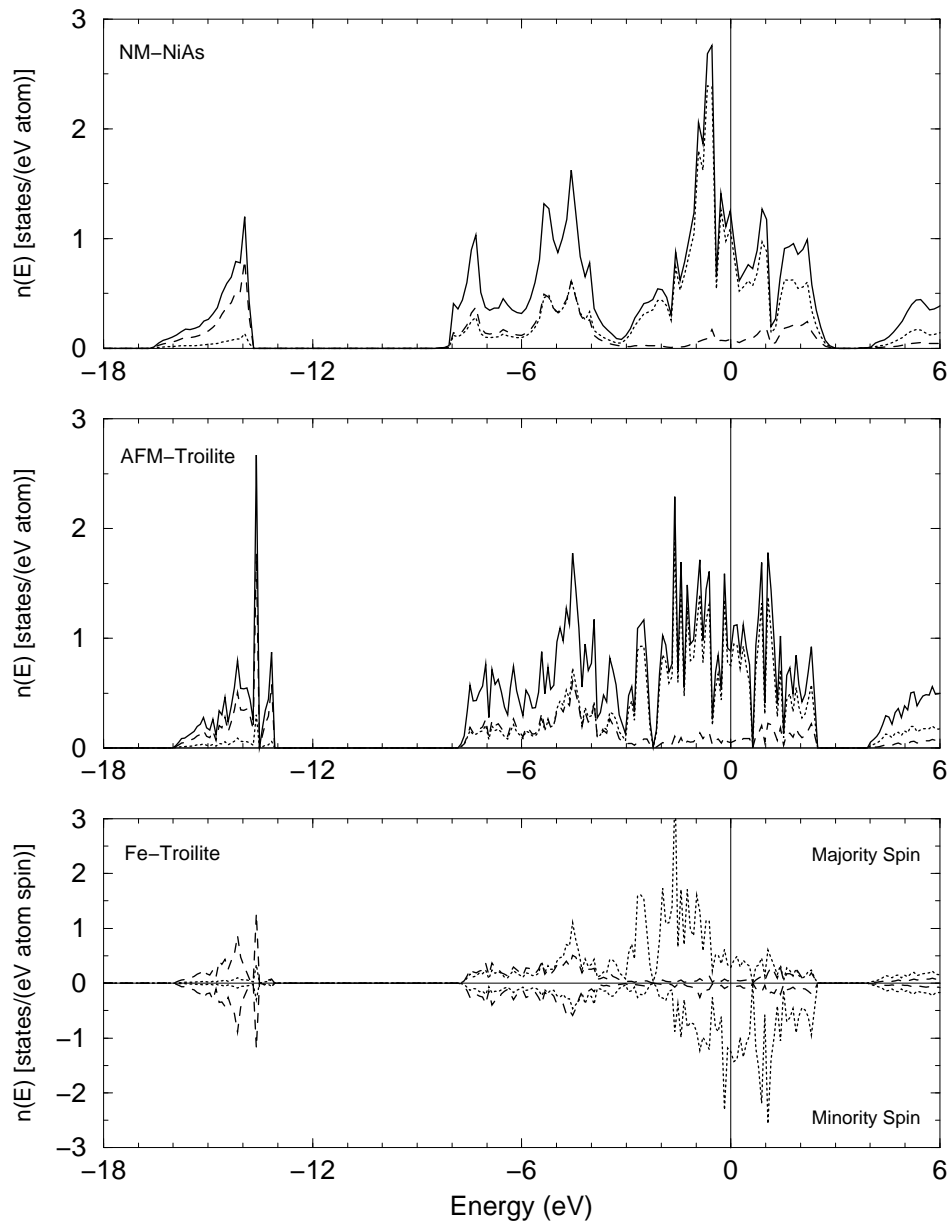
Figure 9. The density of states for the non-magnetic FeS(NiAs type) (upper panel) and the total density of states for the AFM FeS(troilite) (middle) structure. The lower graph shows the spin-polarized local density of states of AFM troilite (dotted line: Mn density of states; dashed line: S density of states).

spectra, apart from a slight underestimate of the width of the gap characteristic of the LDA. The main features of local coordination are common to both pyrite and marcasite FeS_2 crystal types. Each metal atom is surrounded by six nearest-neighbour anions in the form of distorted edge-sharing tetrahedra.

The main difference in the atomic arrangement of the orthorhombic marcasite structure
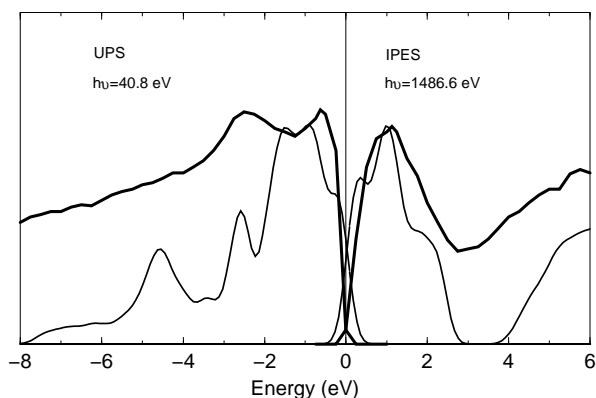
Figure 10. Valence-band photoemission spectra at $h\nu = 40.8$ eV and conduction-band inverse-photoemission spectra at $h\nu = 1486.6$ eV for FeS as measured by Shimada *et al* (bold lines). Superimposed is a rough estimate of the photoemission spectra, using photo-ionization cross-sections, from our calculated density of states of the troilite structure (thin lines).

is that, here, edge sharing of anion octahedra also occurs in linear chains parallel to the orthorhombic *c*-axis. The essential difference in the electronic structure of the marcasite phase is the increased splitting of the t_{2g} orbitals in the less regular octahedral environment [8, 63], but the semiconducting gap is even slightly wider than in the pyrite phase.

In our calculations we have attempted to introduce antiferromagnetic coupling, and our calculations correctly converge to a non-magnetic solution. For the paramagnetic phase we find good agreement between the present all-electron PAW method and the pseudopotential calculations of Raybaud *et al* [7, 8].

3.7. CoS

The NiAs phase of CoS is a Pauli paramagnetic compound at high temperatures [54]. The lack of magnetic ordering in this material is probably related to its small lattice constant $c = 5.16$ Å. As in the case of FeS$_2$, we have again attempted to stimulate antiferromagnetic coupling and correctly found a non-magnetic solution as the ground state.

3.8. CoS$_2$

CoS$_2$ is of the pyrite structure and is a metallic ferromagnetic compound whose Curie temperature, T_c, is about 120 K. The atomic moment is 0.84 μ_B per Co atom [64]. The Co atoms form a face-centred cubic (fcc) structure and sit at the centre of the sulphur octahedron. The strong octahedral crystalline field splits d bands to the lower t_{2g} band and upper e_g band, and the Fermi level lies in the upper e_g band. Due to the cubic structure and the nearly half-filled band, the magnetic Hamiltonian must be isotropic and the anisotropy of the magnetic properties is small. Hiraka *et al* [65] have observed, below T_c, two types of magnetic excitation: spin waves and Stoner excitations. Magnetic excitations above T_c can be explained as an itinerant-electron system, rather than a localized-spin system. High-resolution photoelectron spectra of Fujimori *et al* [59] show a broadening of the characteristic t_{2g} peak located about -1.6 eV below E_F and a less distinct S 3p–Co t_{2g} separation, compared to that for non-magnetic FeS$_2$, attributed to the exchange splitting. The magnetic polarization also leads to a broadening of the unoccupied e_g band as observed in the inverse photoelectron spectroscopy of Muro *et al* [66]. Muro *et al* [66]

have also measured resonant photoemission spectra taken at temperatures across the magnetic transition, indicating a slight but remarkable spectral change between the paramagnetic and ferromagnetic phases.

Our calculations have found a relatively weak magneto-volume effect and a consequent improvement in the calculated atomic volume. As indicated in table 2, we have both a ferromagnetic and an antiferromagnetic solution, the ferromagnetic solution being the ground state in agreement with experiment. The calculated magnetic moment is reasonably close to, but lower (0.76 μ_B) than, the frequently quoted experimental value of 0.85 μ_B (see table 3).

Figure 11 demonstrates that the onset of magnetic ordering is again accompanied by a reduced bond length in the S–S pairs. Our calculated spectra for non-magnetic and ferromagnetic CoS_2 are shown in figure 12. We find that the broadening of the Co t_{2g} band and the decreased separation from the S 3p band are a direct consequence of the weak exchange splitting. Altogether, we find that CoS_2 is well described as a weak itinerant ferromagnet.

3.9. NiS

The NiAs-type NiS exhibits a non-metal–metal transition at a temperature $T_t = 263$ K. Below T_t, it is an antiferromagnetic non-metal with a small charge-transfer gap formed between the highest occupied S 3p band and the lowest unoccupied Ni 3d band. The charge-transfer gap closes at T_t. NiS is a Pauli paramagnetic metal above T_t. Ikoma *et al* [67] and Fujimori *et al* [68, 69] have performed x-ray photoemission experiments at 130 K (i.e. below T_t).

Our calculations have failed to predict the antiferromagnetic ground state reported by experiment. The insulating state of NiS has alternatively been explained as due to a Mott–Hubbard metal/insulator transition or as arising from the formation of an S 3p–Ni 3d charge-transfer gap. Here we merely refer the reader to the discussion in Raybaud *et al* [8], where the low-temperature phase of NiS(millerite) has also been considered.

3.10. NiS₂

The magnetic susceptibility of NiS_2 has an antiferromagnetic behaviour. For NiS_2 the Curie plot breaks into two regions associated with the expansion anomaly at about 400 K leading to effective paramagnetic moments of $\mu_p = 2.70$ μ_B for $T \geqslant 400$ K and $\mu_p = 3.15$ μ_B for $T \leqslant 100$ K. Below the Néel temperature of $T_N = 40$ K, NiS_2 is antiferromagnetic with $\mu_{Ni} = \pm 1.17$ μ_B [70]. Additionally, NiS_2 is suggested to be a Mott insulator to account for the discrepancy between its predicted metallic behaviour and its actual semiconducting behaviour, in spite of its half-filled e_g band. Our calculated ground state is non-magnetic and in disagreement with experiment. Again we refer the reader to the discussion in Raybaud *et al* [8].

4. Discussion

To conclude, we should briefly remark upon the general trends of our calculations. The results tabulated in tables 2 to 4 show that the current formalism predicts the correct ground state of these compounds with the exception of NiS and NiS_2, which are Mott insulators and are beyond the scope of the current framework. In CrS we find a relatively large magneto-volume effect (~7%) and the calculated volume of the antiferromagnetic phase is in rather good agreement with experiment. For MnS we predict an antiferromagnetic semiconducting ground state with a large magneto-volume effect (~21%). Although the final result still underestimates the experimental volume by almost 7%, these calculations represent a drastic improvement on
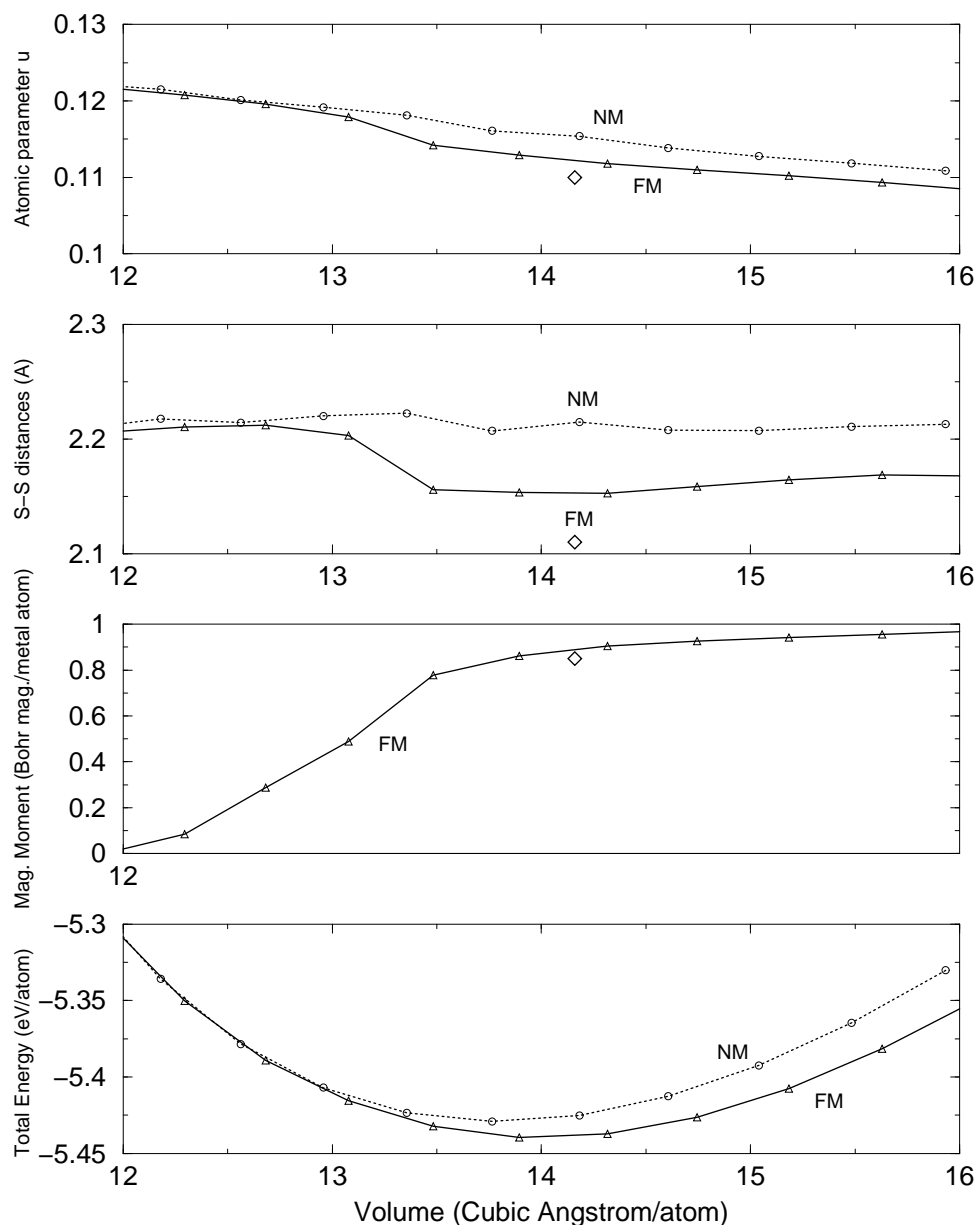
Figure 11. Total energy plotted against volume for non-magnetic and ferromagnetic CoS$_2$. Also shown are the calculated magnetic moments, the S–S distances and the structure parameter u as functions of volume. Experimental data are indicated by diamonds.

previous paramagnetic results which showed an error of almost 28% for the atomic volume. However, the width of the semiconducting gap, the exchange splitting and the magnitude of the magnetic moments are underestimated, indicating that intra-atomic correlation effects are more important in MnS than in CrS (but also distinctly less important than in the antiferromagnetic insulator MnO).
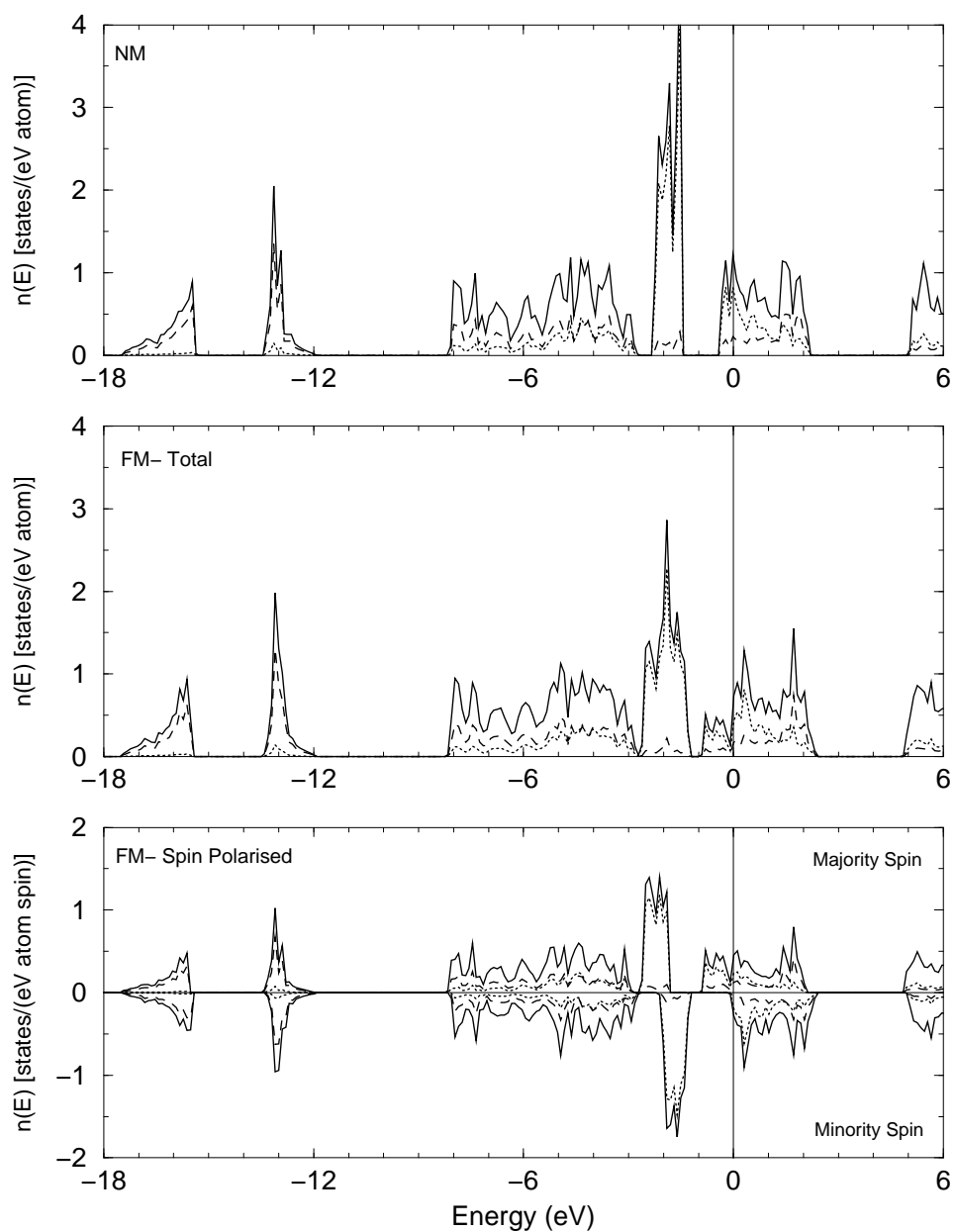
Figure 12. Spin-polarized densities of states for non-magnetic and ferromagnetic CoS$_2$. The format is the same as in the earlier plots of densities of states.

The situation is somewhat more complicated in MnS$_2$ where we find a low-spin antiferromagnetic ground state. However, analysis of the structural and magnetic parameters for this material reveals that the low-spin solution does not conform to the experimental data. For this material we also found a metastable high-spin antiferromagnetic state. We suggest that this is the experimentally relevant structure and the material is then found to have large magneto-volume and magneto-structural effects. The high-spin phase is essentially a zero-gap

semiconductor. The open question is that of the lower stability of the high-spin phase compared to the low-spin phase—as in the case of MnS, we tentatively attribute this discrepancy to the neglect of intra-atomic correlations. Due to the smaller d bandwidth, we expect the correlation effects to be more important in the disulphide than in the monosulphide.

FeS is a complex compound which has a variety of structural and magnetic phase transitions. Our calculations show that NiAs-type FeS is paramagnetic, whereas the troilite phase has an antiferromagnetic ground state. A pressure-induced structural and magnetic phase transition from non-magnetic NiAs type to antiferromagnetic troilite is predicted at a volume reduction of 13%, in good agreement with experiment. However, the calculated magnetic moment appears to be too low compared to a moment close to the Hund's-rule limit of 4 μ_B inferred from the analysis of the magnetic neutron scattering data, and the non-zero density of states at E_F of the minority states disagrees with photoemission and electron specific heat data. Hence intra-atomic correlation effects are also important in FeS. Due to the semiconducting character of FeS_2, non-magnetic phases are stable in this material.

Finally, for the cobalt sulphides we find good agreement with experimental measurements. CoS is a Pauli paramagnet, CoS_2 is ferromagnetic and we have found a weak magneto-volume effect which reduces the error in our calculations of the atomic volume from 3% in the non-magnetic case, to 2% in the magnetic case. For the Ni sulphides, our LSDA + GGA calculations again fail to reproduce the antiferromagnetic insulating ground state created by a Mott–Hubbard transition.

Altogether we find that the tendency towards magnetic ordering and the importance of correlation effects not accounted for in a local density description vary systematically with the filling of the 3d band: VS is non-magnetic, CrS an itinerant antiferromagnet. MnS is correctly described as a high-spin antiferromagnet, but intra-atomic correlation effects are responsible for the high observed exchange splitting. Correlation effects are also necessary to stabilize the high-spin over the low-spin solutions in MnS_2. The structural and magnetic phase transitions in FeS are rather well described in the LSDA + GGA, but correlation effects enhance both magnetic moment and exchange splitting. FeS_2 and CoS are non-magnetic, but semiconducting and metallic, respectively. CoS_2 is a weak itinerant ferromagnet. Correlation effects are extremely important in both Ni monosulphide and disulphide. An important reason for this variation is the pronounced t_{2g}–e_g splitting in the 3d band caused by ligand-field effects. For the pyrite-type disulphides, the strongest correlation effects appear in MnS_2 where in the paramagnetic state the Fermi level falls at the upper edge of a very narrow band of non-interacting t_{2g} states, and in NiS_2 where the e_g band is narrow and well separated from the S $3p\sigma^*$ band. In NiAs-type monosulphides the t_{2g}/e_g splitting is similar, but obscured due to the overlap of the $d_{3z^2-r^2}$ orbitals along the direction of the chain-like arrangement of the metal atoms. Correlation effects are most important if the Fermi level falls close to the peak in the paramagnetic t_{2g} density of states (MnS, FeS) or into a pseudogap in the e_g band (NiS). However, in all cases correlation effects are consistently lower than for the corresponding oxides and a detailed assessment must be left to future work.

References

[1] Topsoe H, Clausen B S and Massoth F 1996 *Hydrotreating Catalysis (Springer Series in Science and Technology vol 11)* (Berlin: Springer)
[2] Anisimov V I, Zaanen J and Andersen O K 1991 *Phys. Rev.* B **44** 943
[3] di Salvo F J and McMillan W L 1977 *Electron–Phonon Interactions and Phase Diagrams* ed T Riste (New York: Plenum) p 107 ff
[4] Wilson J A and Yoffe A D 1969 *Adv. Phys.* **18** 193
[5] Huisman R, de Jounge R, Haas C and Jellinek F 1971 *J. Solid State Chem.* **3** 56
[6] Mattheis L F 1973 *Phys. Rev.* B **8** 3719
[7] Raybaud P, Kresse G, Hafner J and Toulhoat H 1997 *J. Phys.: Condens. Matter* **9** 11 085
[8] Raybaud P, Hafner J, Kresse G and Toulhoat H 1997 *J. Phys.: Condens. Matter* **9** 11 107
[9] Kohn W and Sham L J 1964 *Phys. Rev.* **140** A1133
[10] Jones R O and Gunnarsson O 1989 *Rev. Mod. Phys.* **61** 689
[11] Perdew J P, Chevary J A, Vosko S H, Jackson K A, Pedersen M R, Singh D J and Fiolhais C 1992 *Phys. Rev.* B **46** 6671
[12] Vanderbilt D 1990 *Phys. Rev.* B **41** 7892
[13] Kresse G and Hafner J 1994 *J. Phys.: Condens. Matter* **6** 8245
[14] Kresse G, Furthmüller J and Hafner J 1994 *Phys. Rev.* B **50** 13 181
[15] Moroni E G, Kresse G, Furthmüller J and Hafner J 1997 *Phys. Rev.* B **56** 15 629
[16] Louie S G, Froyen S and Cohen M L 1982 *Phys. Rev.* B **26** 1738
[17] Blöchl P E 1994 *Phys. Rev.* B **50** 17 953
[18] Kresse G and Joubert D 1999 *Phys. Rev.* B **59** 1758
[19] Kresse G and Hafner J 1993 *Phys. Rev.* B **47** 588
[20] Kresse G and Hafner J 1994 *Phys. Rev.* B **49** 14 251
[21] Kresse G and Furthmüller J 1996 *Phys. Rev.* B **54** 11 169
[22] Kresse G and Furthmüller J 1996 *Comput. Mater. Sci.* **6** 15
[23] Pulay P 1980 *Chem. Phys. Lett.* **73** 393
[24] White J A and Bird D M 1994 *Phys. Rev.* B **50** 4954
[25] Monkhorst H J and Pack J D 1976 *Phys. Rev.* B **13** 5188
[26] Blöchl P E, Jepson O and Andersen O K 1994 *Phys. Rev.* B **49** 16 223
[27] Motizuki K, Katoh K and Yanase A 1986 *J. Phys. C: Solid State Phys.* **19** 495
[28] Liu S H 1974 *Phys. Rev.* B **10** 3619
[29] Dijkstra J, van Bruggen C F, Haas C and de Groot R A 1989 *J. Phys.: Condens. Matter* **1** 9163
[30] Goodenough J B 1963 *Magnetism and the Chemical Bond* (New York: Interscience)
[31] Jellinek F 1957 *Acta Crystallogr.* **10** 620
[32] Popma T J A and van Bruggen C F 1969 *J. Inorg. Nucl. Chem.* **31** 73
[33] Turek I, Becker Ch and Hafner J 1992 *J. Phys.: Condens. Matter* **4** 7257
[34] Fender B E F, Jacobson K J and Wedgewood F K 1968 *J. Chem. Phys.* **48** 990
[35] Sato H, Mihara T, Furuta A, Ueda Y, Namatame H and Taniguchi M 1996 *J. Electron Spectrosc. Relat. Phenom.* **78** 87
[36] Duffman D R and Wild R L 1967 *Phys. Rev.* **156** 989
[37] Wei S and Zunger A 1993 *Phys. Rev.* B **48** 6111
[38] Hines R I, Allen N L, Bell G S and Mackrodt W C 1997 *J. Phys.: Condens. Matter* **9** 7105
[39] Pisai C 1996 *Quantum Mechanical ab-initio Calculations of the Properties of Crystalline Materials (Springer Lecture Notes in Chemistry vol 67)* (Berlin: Springer) ch 6
[40] Tappero R, D'Arco P and Lichanot A 1997 *Chem. Phys. Lett.* **173** 83
[41] Tappero R and Lichanot A 1998 *Chem. Phys.* **236** 97
[42] Anisimov V I, Aryasetiawan F and Liechtenstein A I 1997 *J. Phys.: Condens. Matter* **9** 767
[43] Solovyev I V, Liechtenstein A I and Terakura K 1998 *Phys. Rev.* B **58** 15 496
[44] Krajčí M and Hafner J 1999 to be published
[45] Hastings J M and Corliss L M 1976 *Phys. Rev.* B **14** 1995
[46] Chattopadhyay T, Brückel T and Burlet P 1991 *Phys. Rev.* B **44** 7394
[47] Chattopadhyay T, von Schnering H G and Graf H A 1984 *Solid State Commun.* **50** 865
[48] King H E and Prewitt C T 1982 *Acta Crystallogr.* B **38** 1877
[49] Coey J M D and Roux-Buisson H 1979 *Mater. Res. Bull.* **14** 711
[50] Kusaba K, Syono Y, Kikegawa T and Shimomura O 1997 *J. Phys. Chem. Solids* **58** 241
[51] Kusaba K, Syono Y, Kikegawa T and Shimomura O 1997 *J. Phys. Chem. Solids* **59** 945

[52] Shimada K, Mizokawa T, Mamiya K, Saitoh T, Fujimori A, Ono K, Kakizaki A, Ishii T, Shirai M and Kamimura T 1998 *Phys. Rev.* B **57** 8845
[53] Kobayashi H, Sato M, Kamimura T, Sakai M, Onodera H, Kuroda N and Yamaguchi Y 1997 *J. Phys.: Condens. Matter* **9** 515
[54] Ikeda H, Shirai M, Suzuki N and Motizuki K 1993 *Japan. J. Appl. Phys. Suppl.* 3 **32** 301
[55] Shirai M, Suzuki N and Motizuki K 1996 *J. Electron Spectrosc. Relat. Phenom.* **78** 95
[56] Ikeda H, Shirai M, Suzuki N and Motizuki K 1995 *J. Magn. Magn. Mater.* **140–144** 159
[57] Sherman D M 1995 *Earth Planet. Sci. Lett.* **132** 87
[58] Gorter E W and Wojtowicz P J 1968 *J. Appl. Phys.* **39** 896
[59] Fujimori A, Mamiya K, Mizokawa T, Miyadai T, Sekiguchi T, Takahashi H, Môri N and Suga S 1996 *Phys. Rev.* B **54** 16 329
[60] Folkerts W, Sawatzky G A, Haas C, de Groot R A and Hillebrecht F U 1987 *J. Phys. C: Solid State Phys.* **20** 4135
[61] Bocquet A E, Mamiya K, Mizokawa T, Fujimori A, Miyadai T, Takahashi H, Môri M and Suga S 1996 *J. Phys.: Condens. Matter* **8** 2389
[62] Néel L and Benoit R 1953 *C. R. Acad. Sci., Paris* **237** 444
[63] Bullett D W 1982 *J. Phys. C: Solid State Phys.* **15** 6163
[64] Hiraka H and Endoh Y 1994 *J. Phys. Soc. Japan* **63** 4573
[65] Hiraka H, Matsuura M, Yamada K and Endoh Y 1997 *Physica* B **237–238** 478
[66] Muro T, Kimura A, Iwasaki T, Ueda S, Imada S, Matsushita T, Sekiyama A, Susaki T, Mamiya K, Harada T, Kanomata T and Suga S 1998 *J. Electron Spectrosc. Relat. Phenom.* **88–91** 361
[67] Ikoma H, Matoba M, Mikami M and Anzai S 1995 *J. Phys. Soc. Japan* **64** 2600
[68] Fujimori A, Terakura K, Taniguchi M, Ogawa S, Suga S, Matoba M and Anzai S 1988 *Phys. Rev.* B **37** 3109
[69] Fujimori A, Namatame H, Matoba M and Anzai S 1990 *Phys. Rev.* B **42** 620
[70] Wilson J A and Pitt G D 1971 *Phil. Mag.* **23** 1297
[71] Chattopadhyay T, Burlet P, Regnault L P and Rossat-Mignod J 1989 *Physica* B **156–157** 241
[72] Chattopadhyay T, Brückel T, Hohlwein D and Sonntag R 1995 *J. Magn. Magn. Mater.* **140–144** 1759
[73] Shimada K, Mizokawa T, Saitoh T, Mamiya K, Fujimori A, Ono K, Kakizaki A, Ishii T, Shirai M and Kamimura T 1996 *J. Electron Spectrosc. Relat. Phenom.* **44** 317
[74] Hiraka H, Endoh Y and Yamada K 1998 *J. Magn. Magn. Mater.* **177–181** 1349
[75] Goodenough J B 1997 *J. Alloys Compounds* **262–263** 1